Deformation of binary and boron-doped Ni_3Al alloys at high pressures studied with synchrotron X-ray diffraction

S.V. Raju[a,b,*], R.N. Vasin[c], B.K. Godwal[d], R. Jeanloz[d,e], H.-R. Wenk[d] and S.K. Saxena[a]

[a] CeSMEC, Department of Mechanical and Materials Engineering, Florida International University, Miami, FL-33172, USA

[b] Presently at Oak Ridge Associated Universities, Belcamp, MD-21017, USA

[c] Frank Laboratory of Neutron Physics, Joint Institute for Nuclear Research, Dubna- 141980, Russia

[d] Department of Earth and Planetary Science, University of California, Berkeley, CA-94720, USA

[e] Miller Institute for Basic Research in Science and Department of Astronomy, University of California Berkeley, CA-94720, USA

*Corresponding author, email: selvavennila@gmail.com

ABSTRACT:

In-situ X-ray synchrotron diffraction experiments were carried out on nickel-based high-strength superalloys under pressure to understand their deformation mechanism using a diamond anvil cell (DAC). Radial X-ray diffraction determines the room-temperature equations of state and yield strengths of binary Ni_3Al alloy and 500 ppm boron doped Ni_3Al to pressures of 20 and 46 GPa, respectively. Crystallographic preferred orientations (CPOs) observed in these superalloys due to anisotropic stress field in DAC indicate onset of plastic deformation. Inverse pole figure analysis reveals that, the underlying deformation mechanisms changes from octahedral slip to a simultaneous activation of octahedral and cube slip upon doping with Boron. The yield-strength values were found to increase with pressure, are comparable to those determined from axial diffraction experiments. The results indicate that the yield strength of Ni_3Al:B is about 0.5 GPa higher (at pressures below 20 GPa) due to grain boundary strengthening by boron. It is shown that due to high elastic anisotropy of Ni_3Al alloy, yield strength estimations from diffraction experiments strongly depend on micromechanical model used to convert measured elastic strains into stresses.

INTRODUCTION:

Superalloys resist thermal creep deformation, and exhibit excellent mechanical strength, fatigue strength, surface stability and corrosion resistance Reed (2006); Pollock and Tin (2006); Jozwik et al. (2015). Motivated by their wide use in aerospace engineering and other high-temperature industrial applications, much research is aimed at characterizing superalloy structures

and properties, and producing improved superalloys e.g., Sato et al. (2006); Minshull et al. (2011); Makineni et al. (2015a); Makineni et al. (2015b)]. We therefore document the deformation of nickel-based high-strength superalloys under pressure using X-ray synchrotron diffraction with diamond-anvil cells (DAC) in axial and radial geometries, as well as with the pressure-gradient method. Diffraction experiments using axial geometry and a pressure medium determine the equation of state, hence bulk modulus of the sample. Radial DAC (rDAC) experiments without a pressure medium impose anisotropic stresses across the sample, and can thus provide estimates of yield strength Ruoff (1975); Singh (1993). In addition, measurements of pressure gradients across the sample offer a separate means of estimating yield strength under static compression Sung et al., (1977); Meade and Jeanloz (1988).

Previous studies on Ni_3Al, Ni_3Al:B and Ni-Al-Cr alloy were aimed at clarifying crystal structural stability, and the effects of alloying on compressibility and hardness Raju et al. (2015); Raju et al. (2016); Raju et al. (2018). Although several studies have been made in the past on Ni_3Al – due to its high melting point, low density and high oxidation resistance property – its intrinsic brittleness and poor tolerance to damage at room temperature and low creep strength at higher temperatures have hindered its use in various industrial applications. Alloying Ni_3Al with different elements is tested in order to improve its properties. It has been discovered, for example, that micro alloying the stoichiometric Ni_3Al with boron may increase its ductility, with the maximum softening effect reached near 500 ppm boron content Qian and Chow (1992).

These studies reveal that doping Ni_3Al with 500 ppm boron increases the bulk modulus of Ni_3Al by 8% compared to the undoped alloy Raju et al. (2015). High-angle annular dark-field (HAADF) Scanning Tunneling Electron Microscope (STEM) imaging of Ni_3Al:B shows that boron segregates to the grain boundaries, hindering the movement of defects and dislocations between γ' Ni_3Al grains, which correlates with an increase in bulk modulus K and a decrease in shear modulus G relative to the values for pure Ni_3Al Raju et al. (2015). It is found that Ni_3Al:B has the highest K/G value, indicative of high strength and superior ductility, in comparison with binary Ni_3Al and ternary Ni-Al-Cr alloys. Ball and Gottstein (1993) discovered that, after large strain deformation, Ni_3Al +0.24 at.% B alloy is characterized by the development of extremely inhomogeneous structural defects: microband clusters and shear bands. This results in virtually unabated strain hardening.

Motivated by these effects of boron doping, we carry out rDAC synchrotron X-ray diffraction experiments in order to compare the high-pressure deformation of binary Ni_3Al and Ni_3Al:B alloys. Crystallographic preferred orientation(CPO) forms in these superalloys due to anisotropic stresses field in the DAC, indicating the onset of plastic deformation. In contrast to previous work Raju et al. (2018), that used two variants of axial DAC geometry: with an ethanol-methanol pressure

medium, and without a pressure medium, and analyzed the data using Singh et al.'s (1998) model, we now use the "bulk-path-GEO" method Matthies et al. (1994); Matthies et al. (2001a); Matthies et al. (2001b) for rDAC diffraction data analysis. The method uses anisotropic single-crystal elastic properties and crystallographic texture to compute elastic constants and determine effective elastic stresses in the sample.

EXPERIMENTAL DETAILS:

Stoichiometric compositions of elemental powders of Ni_3Al and its alloy with 500ppm boron were made into pellets, and arc melted and solidified under vacuum by directional solidification using the Bridgman-Stockbarger technique. Preliminary analysis of both alloys was carried out by X-ray diffraction (XRD), High-annular angle dark field (HAADF) technique with Scanning Tunneling electron Microscope (STEM) imaging and energy dispersive spectroscopy (EDS) Raju et al. (2015); Raju et al. (2018). The crystal structure of Ni_3Al and Ni_3Al:B alloys determined from both XRD and STEM confirmed formation of $L1_2$-type structure (γ' phase, space group $Pm\bar{3}m$) with lattice parameters 3.572±0.01 Å (unit cell volume 45.476 ± 0.383 $Å^3$) and 3.557 ± 0.005 Å (45.004±0.190 $Å^3$) respectively, in agreement with literature values e.g., Dey (2003).

X-ray diffraction rDAC experiments were carried out at beamline 16IDB of HPCAT, Advanced Photon Source; all data were collected at room temperature. Ni_3Al and Ni_3Al:B (500 ppm) grains of 3-5 μm size were loaded into panoramic diamond-anvil cells in a boron-epoxy gasket enclosed by an outer Kapton sheet Lin et al. (2003); Merkel and Yagi (2005). No pressure-transmitting medium was used, which resulted in shear stresses across the sample. The experimental layout and diamond-cell details are described in Raju et al. (2018). Platinum flakes (~ 10 μm diameter and 5 μm thickness) were mixed with the sample powders to serve as internal pressure standards. Monochromatic X-rays (0.42460 Å wavelength) were focused to a spot size of 10 x 10 μm to collect diffraction images over a 2θ range up to ~ 26° using a MarXperts Mar345 image-plate detector. Sample-to-detector distance (331.29 mm), detector tilt and instrumental resolution were determined using a CeO_2 calibration standard. The sample was compressed using a gas-driven membrane, and the pressure on the sample was determined from the observed lattice parameter of Pt using its equation of state of Matsui et al. (2009).

Selected diffraction patterns are shown in Fig. 1. Images at lower (~ 2 GPa) pressures appear to have higher Pt content than higher-pressure images. This is most likely because the beam cross section is smaller than the sample diameter. During compression, the part of the sample illuminated by the beam shifts slightly, causing a change in the relative intensities of the Pt and sample diffraction peaks. Preferred orientation of Ni_3Al and Ni_3Al:B crystals, observed at lower pressures,

may be due to the fact that samples were synthesized by melt quenching, and relatively coarse grained alloys were extracted from the ingot.

RADIAL DAC X-RAY DIFFRACTION DATA PROCESSING:

To analyze the diffraction data, we used the modified Rietveld method implemented in the MAUD software package Lutterotti et al. (1997), and a standard procedure described in detail by Wenk, et al. (2014). Diffraction images were integrated over incremental 5° azimuth steps, producing 72 conventional diffraction patterns for each image (Figs. 1 and 2). Deviations of the diffraction peak positions from a constant scattering angle 2θ are indicative of strains, in response to macroscopic mechanical stress, and intensity variations are due to preferred grain orientations.

Due to excessive scattering from the gasket materials near the center of the images, and DAC shadow present at higher scattering angles (visible in left side of diffraction images, Fig. 1), the refinement range was restricted to 2θ = 9-21.5°. Extending the range to 25.9° to add more diffraction peaks to the analysis had negligible impact on the refinement results.

All 72 diffraction patterns from each image were processed simultaneously in MAUD. Backgrounds, unit cell parameters of Ni_3Al and Pt and their relative content, microstructure and macroscopic stress-strain models, CPOs were refined.

Rietveld refinement relies on known crystal-structure models. The structure of platinum is face-centered cubic with space-group $Fm\bar{3}m$, but the situation with Ni_3Al alloys is more ambiguous. At ambient conditions, binary Ni_3Al alloy has an ordered γ' phase with $L1_2$ structure and space group $Pm\bar{3}m$ Dey (2003). When compared to the disordered fcc ($Fm\bar{3}m$) structure, characteristic of pure Ni-Al, diffraction patterns of the $L1_2$ structure feature additional superstructure peaks. Among $L1_2$ superstructure peaks, (100) is at the lowest angle where the intensity is dominated by gasket scattering. Thus, it is excluded from the refinement range. Peaks (221) and (300) are overlapped by stronger platinum reflection. Peaks (110), (210) and (211) are separate, and may be identified in the diffraction images. However, these peaks have low intensities [e.g., Ovcharenko et al., 2017], and may be broadened by the presence of antiphase boundaries typical of the $L1_2$ structure [Warren, 1990]. In addition, it has been suggested that plastically deformed Ni_3Al alloy (either binary or boron-doped) may become partially disordered, decreasing the superstructure peaks intensities even further [Horto et al., 1991; Ball and Gottstein, 1994]. The positions of the $L1_2$ (110), (210) and (211) peaks are marked in Figs. 1 and 2. It is evident that a weak (110) Debye ring is present in all diffraction images, showing some preferred orientation. The (210) and (211) peaks are barely visible, which leaves the possibility that the studied Ni_3Al and Ni_3Al:B are in the ordered $L1_2$ structure, or are a mixture of $L1_2$ and a disordered fcc phase.

In Rietveld refinements, we tried two probable structure models, ordered $L1_2$ ($Pm\bar{3}m$) and disordered fcc structure ($Fm\bar{3}m$), as well as an unconstrained mixture of ordered and disordered phases, for Ni_3Al and Ni_3Al:B. A two-phase model statistically resulted in slightly better refinement (lower R-factors and goodness-of-fit values) than disordered fcc model, which is due to the introduction of more free parameters into the refinement, while $L1_2$ was marginally worse. Equations of state and yield strengths derived from refinements using A1 or $L1_2$ structures agree with each other within error margins.

It should be noted that due to the relatively low energy of formation of crystal structures with ordered antiphase boundaries in Ni_3Al alloys, other ordered structures, such as another $L1_2$, $D0_{22}$ or $D0_{23}$ may be stable in Ni_3Al alloys at increased temperatures, under strain, or due to stoichiometry deviations e.g., Ramesh et al. (1994); Kazantseva et al. (2019). Their recognition is not possible in our experiments, and they were not considered.

Popa's (1998) anisotropic peak broadening model was used to take into account diffraction-peak broadening related with anisotropic microstrains in the material, and possibly nonspherical shapes of crystallites that in this model are represented by "composite" crystallites with a shape determined by the Laue class of the crystal lattice.

To account for grain preferred orientations in the refinement, a discrete E-WIMV algorithm was used with 10° cell size in orientation space Matthies (2002); Lutterotti et al. (2014). Textures remain weak and somewhat asymmetric at all pressures, though a change of orientations is observed after the initial compression that remains practically unchanged at higher pressures.

According to the analysis procedures, elastic stresses in the rDAC can be separated into a hydrostatic and a deviatoric part Lutterotti et al. (2014). Only the hydrostatic part (i.e., the pressure) affects unit-cell parameters. Deviatoric stresses cause systematic displacements of the diffraction peaks along the azimuthal angle of Debye rings. The deviatoric stress tensor is diagonal with a zero trace, and $\sigma_{11} = \sigma_{22} = -\sigma_{33}/2$ (where σ_{33} is the stress component along the compression axis), and all other components are equal to zero. The differential stress value t can be derived as $t = \sigma_{33} - \sigma_{11}$. This value corresponds to the maximum shear (Tresca) and, considering the rDAC geometry, to the von Mises yield criterion Ruoff (1975); Singh (1993); it therefore represents the yield strength on compression.

The "bulk-path-GEO" method Matthies et al. (1994); Matthies et al. (2001a); Matthies et al. (2001b) implemented in MAUD accounts for deviatoric stresses in the DAC by combining single-crystal elastic constants and measured CPOs to calculate diffraction elastic constants and estimate macroscopic elastic stresses. The elastic constants of Pt were taken from interpolation of available *ab initio* values Menéndez-Proupin and Singh (2007). Calculations of pressure-dependent elastic constants are also available for the ordered $L1_2$ Ni_3Al alloy Boucetta et al. (2010); and, due to

proximity of C_{11}, C_{12} and C_{44} to the *k*-point mesh in the deformed Brillouin zone, their values increase as the pressure is increased. Most likely, adding 500 ppm boron has little impact on alloy elastic constants, and the same values are used for Ni_3Al:B. There is no information on elasticity of the disordered or partially disordered alloy, which may appear during the course of plastic deformation. Yet, a comparison of Young's moduli of films of ordered and disordered Ni_3Al show that they are nearly equal Huang et al. (2001). Consequently, we assume that the same set of elastic constants can be used for ordered and disordered Ni_3Al, and that our results hold independent of the Ni_3Al ordering.

Refined diffraction patterns (assuming a $L1_2$ structure for Ni_3Al alloys and without imposed texture symmetry) are compared with the experimental data in Fig. 2 . Intensities and positions of diffraction peaks are correctly reproduced, indicating the validity of our texture and stress models.

RESULTS:

Rietveld refinement provided information on CPOs, unit cell parameters and mechanical stresses in Ni_3Al and Ni_3Al:B samples.

Orientation distribution functions were exported from MAUD into Beartex software Wenk et al. (1998) and smoothed using a 10° Gaussian filter. Inverse pole figures for the compression direction and pole figures for several lattice planes were calculated. For initial and maximum pressures, they are shown on projections in Fig. 3 as contours of pole density in multiples of a random distribution (m.r.d.). Texture remains weak at all pressures for both Ni_3Al and Ni_3Al:B, and demonstrates evident deviation from fiber symmetry. Maximum values on inverse pole figures are below 1.8 m.r.d., while minimum values are over 0.4 m.r.d. (Fig. 3), indicating the presence of large random texture component. The change of initial preferred orientations is observed at pressures over 10 GPa: a weak preferred orientation of {110} planes normal to compression is formed in binary Ni_3Al, while in Ni_3Al:B a weak {210} alignment is observed.

Unit cell parameters for Ni_3Al and Ni_3Al:B at several pressures were extracted from Rietveld refinement, and dependencies of unit-cell volumes of the studied alloys on pressure were plotted as functions of pressure (Fig. 4) and fitted with the Birch-Murnaghan equation of state Birch (1947). Because of the limited pressure range and number of data points, the bulk-modulus pressure derivative was fixed at 4, as in previous research Raju et al. (2018). As expected, Ni_3Al:B has a higher bulk modulus and lower unit-cell volume at zero pressure, as compared to the undoped alloy (Table 1).

Differential stress values *t*, characterizing anisotropic stresses in the DAC, are plotted in Fig. 5. There is a rapid increase of *t* at pressures up to ~10 GPa that is followed by a more gradual increase at higher pressures. For Ni_3Al:B, high pressure measurements show that differential stress

t increases to ≈4.7 GPa at 32 GPa, and remains practically constant up to 46 GPa pressure. Overall, boron-doped alloy is characterized by higher *t* values.

DISCUSSION:

Compression of Ni_3Al alloy was studied by different experimental and modeling techniques, and obtained bulk modulus values are summarized in Table 1. Available *ab initio* calculations show a large spread. Bulk modulus values obtained in the present study are well below the results of other DAC experiments, both hydrostatic (with pressure medium) and non-hydrostatic, and are closer to ultrasonic wave-propagation and resonant-frequency measurements at ambient conditions Frankel et al. (1986); Prikhodko et al. (1999). Our measurements and Birch-Murnaghan fit follow the expected gradual decrease of unit cell volume with pressure (Fig. 4), and do not support earlier indications of a compression anomaly for Ni_3Al at pressures over 5 GPa Otto et al. (1998); Otto et al. (2000).

During rDAC experiment, compression induces deviatoric mechanical stresses and promotes formation of CPO. Under compression, an fcc metal is expected to deform mostly by {111}<110> octahedral slip, aligning {110} planes normal to compression Rollet and Wright (1998). In superalloys with the ordered $L1_2$ structure, this deformation mode at low temperatures is hindered by dislocation cross slip onto {110} planes Ezz et al. (1982); Dey (2003). It is established that deformation twinning is inactive in boron-doped Ni_3Al Ball and Gottstein (1993), as well as in binary Ni_3Al alloy Kishida et al. (2004); Kaneno et al. (2006). In binary and boron-doped Ni_3Al alloys, formation of shear and slip bands have been observed in deformation experiments Horto et al. (1991); Ball and Gottstein (1993). In ordered boron-doped Ni_3Al alloy, texture develops rapidly, but remains weak compared to disordered materials Ball et al. (1991). The developed texture depends on initial microstructure, and may be inhomogeneous in coarse-grained alloy. It was reported that rolling textures of boron-doped Ni_3Al have a significant random component, large spread of main texture components and the pole figures are somewhat asymmetric Ball and Gottstein (1993); Ball and Gottstein (1994).

In our experiments, crystallographic textures of Ni_3Al and Ni_3Al:B (Fig. 3) remains weak and asymmetric at all pressures. Yet, the initial preferred orientation patterns show evident change due to axial compression. In binary Ni_3Al, a weak alignment of {110} planes normal to compression is observed, which is consistent with deformation by {111}<110> slip. In Ni_3Al:B, we observe a weak maximum at {210} on inverse pole figure. Taylor type models of texture development in $L1_2$ polycrystals in compression suggest that this is due to simultaneous activation of octahedral and cube {001}<110> slip Raabe (1995). It is quite peculiar, as at ambient pressure cube slip in $L1_2$

polycrystals is mainly active at high temperatures, where a negative temperature dependence of strength is observed.

Noticeable changes of preferred orientations are at pressures ~ 10 GPa, indicating the onset of the plastic deformation due to increasing differential stress *t*. If the yield strength of the material is relatively high, it may be expected that at lower pressures (and differential stresses well below the yield strength), the deformation of the material would be elastic and *t* values would rapidly increase with increasing pressure until the yield strength is reached. After that, a slower increase of *t* with pressure would be observed, corresponding to the pressure-driven increase of yield strength. Consequently, it is reasonable to assume that the values obtained for differential stress *t* correspond to maximum shear/von Mises-criterion strength only at pressures above ~10 GPa, at which *t* values are over 3 GPa.

Let us review how these values of *t* compare to available estimates for the yield strength of Ni_3Al.

It should be noted that even though plastic deformation of superalloy single crystals is characterized by tension-compression asymmetry, e.g., Ezz et al. (1982); Nitz et al. (1998), in weakly textured polycrystals this effect should be suppressed due to directional dependence of its sign Schulson et al. (1985).

Also it is known that the strength of Ni_3Al alloys is affected by grain size: decreasing grain size significantly increases tensile strength Ovcharenko et al. (2017) and yield strength Schulson et al., (1985). In Ni_3Al yield strength is linearly related to $D^{-0.8}$ (where D is the grain size), while in the more usual Hall-Petch relation yield strength is proportional to $D^{-0.5}$ Schulson et al., (1985).

The yield strength of ~ 0.9 GPa is expected for binary Ni_3Al with D = 3 μm at ambient conditions Schulson, et al. (1985). Ball and Gottstein (1994) determined yield strength of 0.24 at.% boron doped Ni_3Al to be 0.805 GPa for the alloy with recrystallized grain size of 2 μm, and 0.665 GPa for the alloy with D = 3.5 μm. Otto et al. (2000) estimated the yield strength of Ni_3Al on compression to be 6-12 GPa, arguing that this could be due to sub-μm grain sizes in their experiments. In our experiments, initial D values were 3-5 μm, and the estimates for the yield strength are significantly higher than it is expected for the alloy with such grain size. It has been shown that the von Mises yield criterion overestimates the real yield stress for the Ni_3Al based alloy Chen et al. (2012), but this overestimation is ~ 0.1 GPa, and cannot explain the difference between our results and reported yield strength values. Additionally, there may be a dependence of overall yield strength on the ordering state of the alloy, which can become partially disordered during plastic deformation Horto et al. (1991); Ball and Gottstein (1994). However, local disordering of Ni_3Al based alloy was found to lead to transition from homogeneous slip deformation to local

banding that would facilitate the plastic deformation. Therefore, there should be different reasons for the high yield strength estimates from our experiments.

First, in Ni_3Al alloys there may be a quick pressure-driven increase of the yield strength during the initial pressure increase, which is then changed to more gradual, or even near zero, as in Ni_3Al:B at high pressures.

Second, grain size could be decreased during deformation, thus increasing the yield strength. From the dependence of yield strength on grain crystallite size determined by Schulson, et al. (1985), it follows that a grain crystallite size of 0.50 μm would correspond to a yield strength of ~ 3.7 GPa (maximum t value reached for Ni_3Al, see Fig. 5); and a grain size of ~ 0.36 μm would mean a yield strength of ~ 4.8 GPa (maximum t value reached for Ni_3Al:B, see Fig. 5). Thus, the increase in differential stress t with pressures may be due to grain-size reduction to sub-μm sizes. We note that these sizes are still quite large, and such grains may consist of multiple coherently scattering domains making it impossible to use methods of diffraction line profile analysis for grain size estimations.

Finally, yield strength values derived from the diffraction data depend on the micromechanical models relating strains to stresses. In the present study, we used the diamond-anvil cell in radial geometry, and analyzed the diffraction data with MAUD software using the bulk-path-GEO model that considers the influence of CPO on diffraction elastic constants. For Ni_3Al alloy, this approach provides higher differential stress values and higher yield-strength estimates than the analysis of diffraction measurements performed in DAC axial geometry with and without pressure medium Raju et al. (2018) made using the Singh model Singh et al. (1998) to extract lattice strains, deviatoric stresses and estimate yield strength. The differences are of ~1 GPa order. The method of Singh et al. (1998) neglects texture. In order to assess the effect of texture on refined differential stress values, we compared results of our diffraction data analysis obtained by considering measured crystallites preferred orientations to calculate diffraction elastic constants with bulk-path-GEO, and considering a random orientation distribution of alloy grains in this calculation. The differences between random texture model and the model with measured texture are generally within ~0.1 GPa.

Another important aspect of differences between bulk-path-GEO and Singh approaches is related to different micromechanical assumptions present in these models, explicitly or implicitly. The Singh model features a weighted combination of Reuss (same stress in all grains) and Voigt (same strain) models to calculate diffraction elastic constants for different lattice planes Singh et al. (1998). Bulk-path-GEO utilizes a geometric mean average of material elastic constants, not only for the diffraction elastic constants from every peak, but also for the full bulk material, ensuring the compatibility of computed elastic properties of the material by exactly obeying the so-called

inversion relation, i.e., that stiffness is the inverse compliance Matthies et al. (2001b). It has been shown that elastic constants derived from the Singh et al. (1998) and bulk-path-GEO approximations are different Matthies et al. (2001a). Differences between micromechanical models are larger when the material is weakly textured (or isotropic). Consequently, values of stress and yield strength obtained using Singh and bulk-path-GEO approximations are expected to be different too. To highlight the influence of different micromechanical models on an estimation of differential stress (an yield strength) in Ni_3Al and Ni_3Al:B, we also performed diffraction data analysis using Voigt and Reuss micromechanical models instead of bulk-path-GEO to calculate diffraction elastic constants. These two models represent upper and lower boundaries for the elastic properties of the polycrystal, and it may be considered that all estimations of t values should lie between those obtained using Voigt and Reuss models. Fig. 5 shows that there is a large possible spread of t values. It is due to high elastic anisotropy of Ni_3Al Boucetta et al. (2010). E.g., at ambient pressure, difference between minimum and maximum Young's moduli of single crystal Ni_3Al is over 3 times. This difference increases with pressure. Consequently, e.g., at a pressure of 19.7 GPa (maximum pressure reached in experiment with binary Ni_3Al), the difference between Ni_3Al isotropic Young's moduli calculated using Voigt and Reuss models is $\approx$ 2.4 times (342 GPa and 167 GPa, correspondingly). Therefore, we observe significantly different t values derived by using Voigt and Reuss micromechanical models to calculate diffraction elastic constants (Figure 5).

It should be noted that different models relating diffraction peak shifts to mechanical stresses are indistinguishable in terms of diffraction data refinement quality Matthies et al. (2001a). Hence, it is impossible to select a correct model to estimate yield strength values using diffraction data only. The applicability of any given model can be decided only based on the analysis of microstructure (such as grain shapes, correlations in positions and orientations, presence of bands or clustering, etc.).

CONCLUSION:

Synchrotron X-ray diffraction experiments using the radial-diffraction diamond-anvil cell (rDAC) technique were carried out to obtain the room-temperature equations of state and yield strengths of Ni_3Al and boron-doped Ni_3Al:B alloys. A bulk modulus value of 161.5(2.9) GPa was obtained for Ni_3Al, which is lower than previous axial DAC results, but comparable to ultrasonic and resonant-frequency measurements. The bulk modulus of 500 ppm boron doped Ni_3Al is found to be 184.0 GPa, which is higher than that of Ni_3Al. Crystallographic texture in axially compressed Ni_3Al and Ni_3Al:B is found to be rather weak and asymmetric. Inverse pole figure of compression direction of Ni_3Al alloy are consistent with deformation by {111}<110> octahedral slip, while preferred orientation in Ni_3Al:B suggests a simultaneous activation of octahedral and cube slip.

Based on deviatoric elastic stress tensor components, calculated using bulk-path-GEO model, maximum shear/von Mises strength estimates are ~ 3.7 GPa at 19.6 GPa pressure for Ni_3Al and ~ 4.8 GPa at 45.8 GPa pressure for Ni_3Al:B. These values are significantly higher than those reported in other experiments for Ni_3Al based alloys with similar grain sizes. It is suggested that this is due to grain size reduction in the course of high pressure experiment, or due to choice of the micromechanical model used to relate strain (diffraction peak shifts) to mechanical stresses due in highly elastically anisotropic material. Therefore, further experiments with a focus on additional microstructure studies are important for correct estimation of yield strength of Ni_3Al based alloys from high-pressure diffraction experiment data.

ACKNOWLEDGEMENTS:

The authors SVR and SKS acknowledge Air Force Office of Scientific Research Grant No. FA9550-12-1-0456 for financial support. HPCAT operations are supported by DOE-NNSA under Award No. DE-NA0001974 and DOE-BES under Award No. DE-FG02-99ER45775, with funding for partial instrumentation by the National Science Foundation. RJ acknowledges support from DOE/NNSA and the University of California. We thank Dr. Chenyong Park, beamline scientist at 16-BMD for valuable support at APS. The Advanced Photon Source is a U.S. Department of Energy (DOE) Office of Science User Facility operated by Argonne National Laboratory under Contract No. DE-AC02-06CH11357. Axial diffraction results are extracted from previous experiments carried out at beamline 12.2.2, Advanced Light Source (ALS), Lawrence Berkeley National Laboratory. ALS is supported by the Director, Office of Science, and Office of Basic Energy Sciences, of the DOE under Contract No. DE-AC02-05CH11231. The authors thank two anonymous referees for their valuable comments that helped to greatly improve the manuscript.

Data availability statement:

Data available on request from the authors	The data that support the findings of this study are available from the corresponding author upon reasonable request.
Data available in article or supplementary material	The data that supports the findings of this study are available within the article.

REFERENCES:

Ball J. and Gottstein G., "Large strain deformation of Ni_3Al+B: Part I. Microstructure and texture evolution during rolling," Intermetallics **1**, 171-185 (1993).

Ball J. and Gottstein G., "Large-strain deformation of Ni_3Al+B: Part III. Microstructure, long-range order and mechanical properties of deformed and recrystallized Ni_3Al+B," Intermetallics **2**, 205-219 (1994).

Ball J., Zeumer B., and Gottstein G., "Microstructure and texture development in boron doped Ni_3Al," Textures and Microstructures **14-18**, 653-658 (1991).

Birch F., "Finite elastic strain of cubic crystals," Phys. Rev. **71(11)**, 809-824 (1947).

Boucetta S., Chihi T., Ghebouli B., and Fatmi M., "First-principles study of the elastic and mechanical properties of Ni_3Al under high pressure," Materials Science-Poland **28(1)**, 347-355 (2010).

Chen L., Wen W., and Cui H., "Yielding description for a Ni_3Al based intermetallic alloy," Materials and Design **41**, 192-197 (2012).

Dey G.K. , "Physical metallurgy of nickel aluminides," Sadhana **28**, 247-262 (2003).

Ezz S.S., Pope D.P., and Paidar V., "The tension/compression flow stress asymmetry in Ni_3(Al,Nb) single crystals," Acta Metallurgica **30(5)**, 921-926 (1982).

Frankel J., Vassiliou J., Jamieson J.C., Dandekar D.P., and Scholz W., "The elastic constants of Ni_3Al to 1.4 GPa," Physica **139-140B**, 198-201 (1986).

Horto J.A., Baker I., and Yoo M.H., "Slip-plane disordering in stoichiometric Ni_3Al," Philosophical Magazine A **63(2)**, 319-335 (1991).

Huang Y., Aziz M.J., Hutchinson J.W., Evans A.G., Saha R., and Nix W.D., "Comparison of mechanical properties of Ni_3Al thin films in disordered fcc and ordered $L1_2$ phases," Acta Materialia **49**, 2853-2861 (2001).

Jozwik P., Polkowski W., and Bojar Z., "Applications of Ni_3Al based intermetallic alloys – Current stage and potential perceptivities," Materials **8**, 2537-2568 (2015).

Iotova D., Kioussis N., and Lim S.P., "Electronic structure and elastic properties of the Ni_3X (X=Mn, Al, Ga, Si, Ge) intermetallics," Physical Review B **54(20)**, 14413-14422 (1996).

Kaneno Y., Takahashi A., and Takasugi T., "Cold rolling texture of Ni-based $L1_2$ ordered intermetallic alloys," Materials Transactions **47(6)**, 1485-1491 (2006).

Kazantseva N.V., Stepanova N.N., and Rigmant M.B., "Superalloys. Analysis and control of failure process," CRC press, Taylor & Francis Group, Boca Raton, FL, USA (2019).

Kishida K., Demura M., Kobayashi S., Xu Y., and Hirano T., "Microstructure and texture evolution during cold rolling and recrystallization of Ni3Al single crystals," Defects and Diffusion Forum **233-234**, 37-48 (2004).

Lin J.-F., Shu J., Mao H.-k., Hemley R.J., and Shen G., "Amorphous boron gasket in diamond anvil cell research," Review of Scientific Instruments **74(11)**, 4732-4736 (2003).

Lutterotti L., Matthies S., Wenk H.-R., Schultz A.S. and Richardson J.W., "Combined texture and structure analysis of deformed limestone from time-of-flight neutron diffraction spectra," Journal of Applied Physics **81**, 594-600 (1997).

Lutterotti L., Vasin R., and Wenk H.-R., "Rietveld texture analysis from synchrotron diffraction images. I. Calibration and basic analysis," Powder Diffraction **29(1)**, 76-84 (2014).

Makineni S.K., Nithin B., and Chattopadhyay K., "A new tungsten-free γ–γ' Co–Al–Mo–Nb-based superalloy," Scripta Materialia **98**, 36-39 (2015a).

Makineni S.K., Nithin B., and Chattopadhyay K., "Synthesis of a new tungsten-free γ–γ' cobalt-based superalloy by tuning alloying additions," Acta Materialia **85**, 85-94 (2015b).

Matsui M., Ito E., Katsura T., Yamazaki D., Yoshino T., Yokoyama A., and Funakoshi K.-I, "The temperature-pressure-volume equation of state of platinum," Journal of Applied Physics **105**, 013505 (2009).

Matthies S., "20 years WIMV, history, experience and contemporary developments," Materials Science Forum **408-412**, 95-100 (2002).

Matthies S., Humbert M., and Schuman Ch., "On the use of the geometric mean approximation in residual stress analysis," Physica Status Solidi (b) **186 (2)**, K41-K44 (1994).

Matthies S., Merkel S., Wenk H.-R., Hemley R.J., and Mao H.-k., "Effects of texture on the determination of elasticity of polycrystalline ε-iron from diffraction measurements," Earth and Planetary Science Letters **194(1-2)**, 201-212 (2001a).

Matthies S., Priesmeyer H.G., Daymond M.R., "On the diffractive determination of single-crystal elastic constants using polycrystalline samples," Journal of Applied Crystallography **34**, 585-601 (2001b).

Mauer F.A., Munro R.G., Piermarini G.J., Block S., and Dandekar D.P., "Compression studies of a nickel-based superalloy, MAR-M200, and of Ni_3Al," Journal of Applied Physics **58(10)**, 3727-3730 (1985).

Meade C. and Jeanloz R., "Yield strength of MgO to 40 GPa," Journal of Geophysical Research **93(B4)**, 3261-3269 (1988).

Menéndez-Proupin E., and Singh A.K., "Ab initio calculations of elastic properties of compressed Pt," Phys. Rev. B **76**, 054117 (2007).

Merkel S. and Yagi T., "X-ray transparent gasket for diamond anvil cell high pressure experiments," Review of Scientific Instruments **76**, 046109 (2005).

Minshull J.P., Neumeier S., Tucker M.G., and Stone H.J., "A1-$L1_2$ structures in the Al-Co-Ni-Ti quaternary phase system," Advanced Materials Research **278**, 399-404 (2011).

Nitz A., Lagerpusch U., Nembach E., "CRSS anisotropy and tension/compression asymmetry of a commercial superalloy," Acta Materialia **46(13)**, 4769-4779 (1998).

Otto J.W., Vassiliou J.K., and Frommeyer G., "Non-hydrostatic conditions in high-pressure devices: Analysis of plastic deformation with EDX," Rev. High Pressure Sci. Technol. **7**, 1511-1513 (1998).

Otto J.W., Vassiliou J.K., and Frommeyer G., "Elastic and plastic deformation of NaCl and Ni_3Al polycrystals during compression in a multi-anvil apparatus," High Pressure Research **17**, 13-34 (2000).

Ovcharenko V.E., Boyangin E.N., Pshenichnikov A.P., and Krilova T.A., "Structural-phase state and strength properties of pressure-synthesized Ni_3Al intermetallic compound," Materials Science Forum **906**, 95-100 (2017).

Pollock T.M. and Tin S., "Nickel-based superalloys for advanced turbine engines: chemistry, microstructure and properties," Journal of Propulsion and Power **22(2)**, 361-374 (2006).

Popa N.C., "The (hkl) dependence of diffraction-line broadening caused by strain and size for all Laue groups in Rietveld refinement," Journal of Applied Crystallography **31(2)**, 176-180 (1998).

Prikhodko S.V., Carnes J.D., Isaak D.G., Yang H., and Ardell A.J., "Temperature and composition dependence of the elastic constants of Ni_3Al," Metallurgical and Materials Transactions A **30A**, 2403-2408 (1999).

Qian X.R. and Chou Y.T. Alloy softening in Ni_3Al polycrystals. Journal of Materials Science **27**, 1036-1044 (1992).

Raabe D., "Modelling of active slip systems, Taylor factors and grain rotations during rolling and compression deformation of polycrystalline intermetallic $L1_2$ compounds," Acta Metal. Mater. **43(4)**, 1531-1540 (1995).

Raju S.V., Oni A.A., Godwal B.K., Yan J., Drozd V., Srinivasan S., LeBeau J.M., Rajan K., and Saxena S.K., "Effect of B and Cr on elastic strength and crystal structure of Ni_3Al alloys under high pressure," Journal of Alloys and Compounds **619**, 616-620 (2015).

Raju S.V., Godwal B.K., Yan J., Jeanloz R., and Saxena S.K., "Yield strength of Ni-Al-Cr superalloy under pressure," Journal of Alloys and Compounds **657**, 889-892 (2016).

Raju S.V., Godwal B.K., Singh A.K., Jeanloz R., Saxena S.K., "High-pressure strengths of Ni_3Al and Ni-Al-Cr," Journal of Alloys and Compounds **741**, 642-647 (2018).

Ramesh R., Pathiraj B. and Kolster B.H., "TEM and high-temperature X-ray diffractometric studies on the structural transformations in Ni_3Al," Journal of Materials Science **29**, 4764-4770 (1994).

Reed R.C., "The superalloys: Fundamentals and applications," Cambridge: Cambridge University Press (2006).

Rollett A.D. and Wright S.I., "Typical textures in metals. In: Texture and Anisotropy," eds. Kocks U.F., Tomé C.N., and Wenk H.-R., Cambridge University Press, UK, pp. 178-238 (1998).

Ruoff A.L., "Stress anisotropy in opposed anvil high-pressure cells," Journal of Applied Physics **46**, 1389-1392 (1975).

Sato J., Omori T., Oikawa K., Ohnuma I., Kainuma R., and Ishida K., "Cobalt-base high-temperature alloys," Science **312**, 90-91 (2006).

Schulson E.M., Weihs T.P., Viens D.V., and Baker I., "The effect of grain size on the yield strength of Ni_3Al," Acta Metallurgica **33(9)**, 1587-1591 (1985).

Singh A.K., "The lattice strains in a specimen (cubic system) compressed nonhydrostatically in an opposed anvil device," Journal of Applied Physics **73**, 4278-4286 (1993).

Singh A.K., Balasingh C., Mao H.-k., Hemley R.J., and Shu J., "Analysis of lattice strains measured under nonhydrostatic pressure," Journal of Applied Physics **83(12)**, 7567-7575 (1998).

Sung C.-M., Goetze C., and Mao H.-K., "Pressure distribution in the diamond anvil press and the shear strength of fayalite," Rev. Sci. Instrum. **48(11)**, 1386-1391 (1977).

Warren B.E., "X-ray diffraction," Dover Publications Inc., New York, USA (1990).

Wenk H.-R., Lutterotti L., Kaercher P., Kanitpanyacharoen W., Miyagi L., and Vasin R., "Rietveld texture analysis from synchrotron diffraction images. II. Complex multiphase materials and diamond anvil cell experiments," Powder Diffraction **29(3)**, 220-232 (2014).

Wenk H.-R., Matthies S., Donovan J., and Chateigner D., "BEARTEX: a Windows-based program system for quantitative texture analysis," Journal of Applied Crystallography **31**, 262-269 (1998).

TABLES:

Table 1. Bulk modulus and its pressure derivative obtained in different experiments and calculations. Asterisk denotes assumed (fixed) value.

Material	K, GPa	K′	Reference	Method
Ni_3Al	161.5(2.9)	4*	This study	Synchrotron diffraction with rDAC
	173.9	--	Prikhodko et al. (1999)	Rectangular parallelepiped resonance
	169	4.4	Frankel et al. (1986)	Ultrasonic measurements
	130.13	8.67	Boucetta et al. (2010)	*Ab initio* calculations
	234	--	Iotova et al. (1996)	*Ab initio* calculations
	185	--	Mauer et al. (1985)	Energy dispersive X-ray with DAC (hydrostatic)
	186.3(6.1)	4*	Raju et al. (2015)	Synchrotron diffraction with DAC (hydrostatic)
	205.5(2.9)	4*	Raju et al. (2018)	Synchrotron diffraction with axial DAC (hydrostatic)
	194.1(3.9)	4*	Raju et al. (2018)	Synchrotron diffraction with rDAC (hydrostatic)
Ni_3Al:B	184.0(3.6)	4*	This study	Synchrotron diffraction with rDAC
	201.8(3.7)	4*	Raju et al. (2015)	Synchrotron diffraction with axial DAC (hydrostatic)

FIGURE CAPTIONS:

Fig. 1. X-ray synchrotron diffraction images of Ni_3Al and Ni_3Al:B in room-temperature radial diamond-cell (rDAC) experiments at different pressures. Some complete Debye rings are indexed, and asterisks mark superstructure reflections of $L1_2$ Ni_3Al. Compression direction is shown by an arrow. Shadows from the beamstop and elements of the DAC (left side of all images) are visible.

Fig. 2. "Unrolled" experimental diffraction images (lower halves, 72 diffraction patterns) and corresponding Rietveld refinements (upper halves, 72 diffraction patterns) assuming fully ordered $L1_2$ Ni_3Al and Ni_3Al:B structures. All the intense diffraction peaks present in the patterns are the same as those indexed in Fig. 1. Positions of superstructure (110), (210) and (211) peaks for $L1_2$ Ni_3Al are indicated. Compression direction is shown by arrows (at 0 and 180°, correspondingly).

Fig. 3. Inverse pole figures for the compression direction and pole figures 100, 110 and 111 for Ni_3Al and Ni_3Al:B. On pole figures, compression direction is in the center, and synchrotron beam is directed bottom-to-top. Equal-area projections with linear scale contours in multiples of a random distribution (m.r.d.). Texture strength is expressed as m.r.d, where higher m.r.d. number represents stronger texture.

Fig. 4. Unit-cell volume dependencies on pressure using rietveld analysis for Ni_3Al (■) and Ni_3Al:B (▲); solid lines are fits to the Birch-Murnaghan equation of state. Standard errors for pressure and volume values are smaller than the size of symbols.

Fig. 5. Differential stress t as a function of pressure for Ni_3Al and Ni_3Al:B as derived using bulk-path-GEO model. Statistical uncertainties of t values obtained in Rietveld refinement are

comparable to size of symbols. Results obtained using Reuss and Voigt models are also shown, and the area between these two models is shaded.

TABLE CAPTION:

Table 1. Bulk modulus and its pressure derivative obtained in different experiments and calculations. Asterisk denotes assumed (fixed) value.

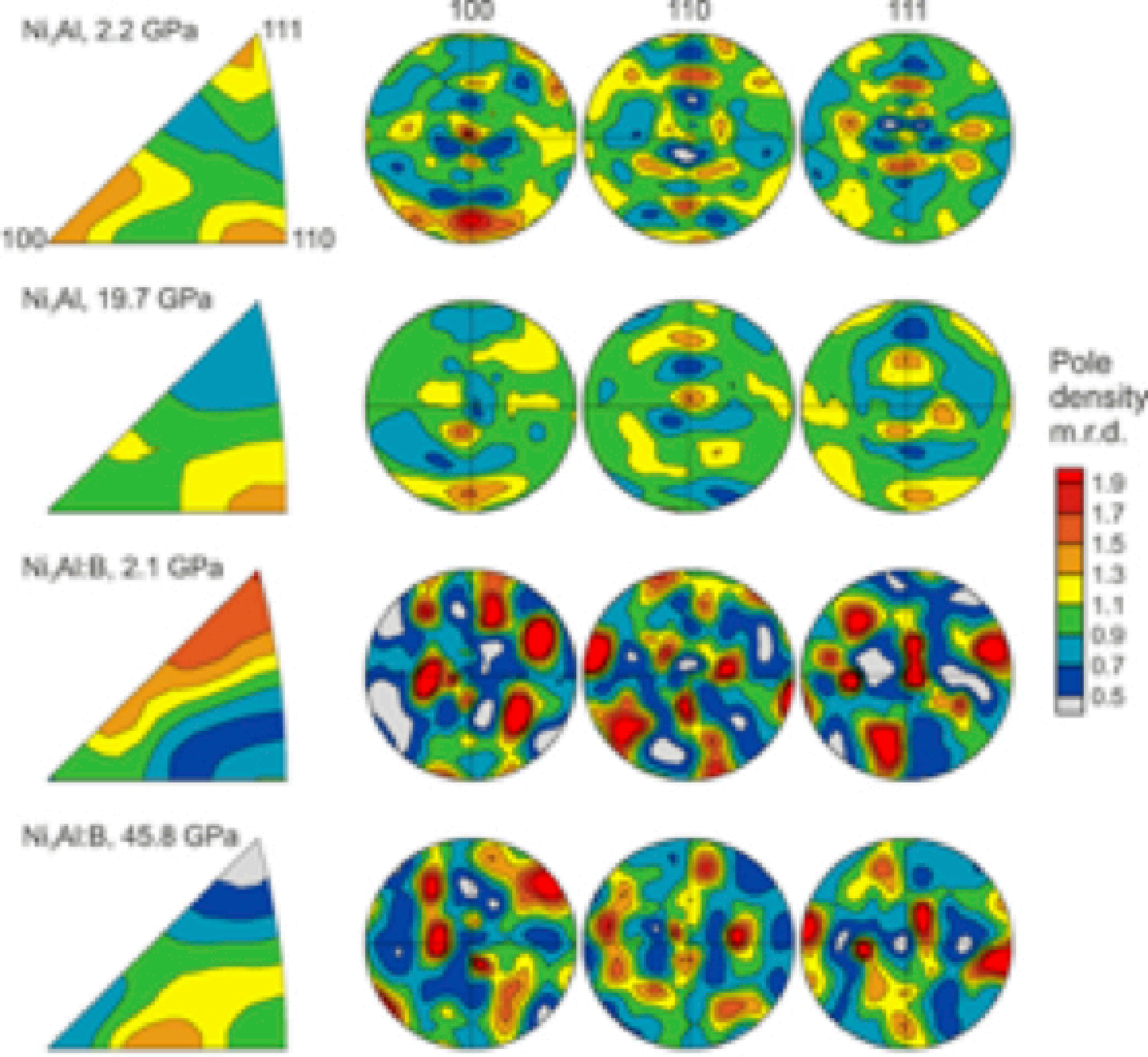
100
110
111
Ni3Al, 2.2 GPa
111
100
110
Ni3Al, 19.7 GPa
Ni3Al:B, 2.1 GPa
Ni3Al:B, 45.8 GPa
Pole density m.r.d.
1.9
1.7
1.5
1.3
1.1
0.9
0.7
0.5

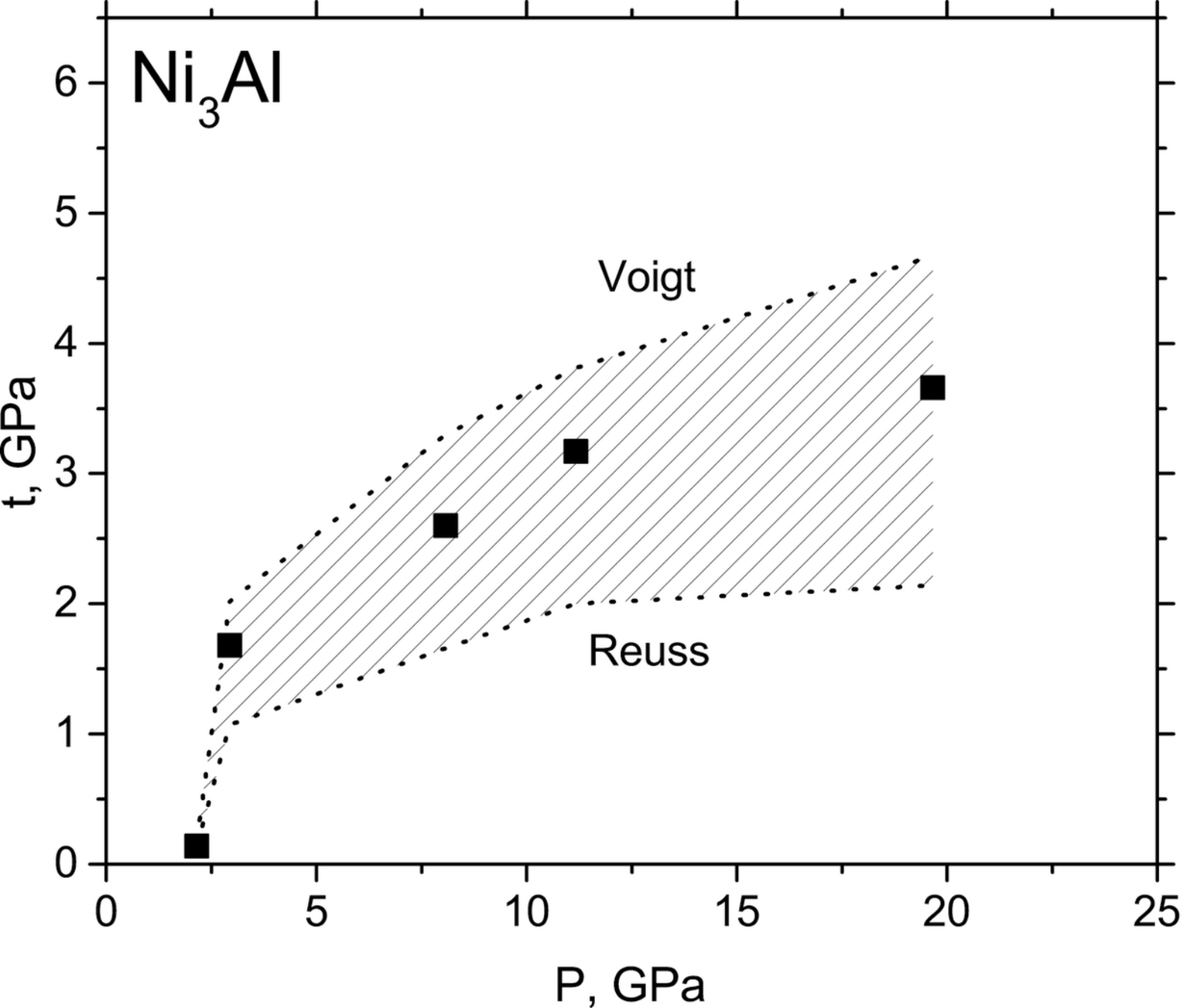
Ni3Al
Voigt
Reuss
t, GPa
P, GPa
0
1
2
3
4
5
6
0
5
10
15
20
25

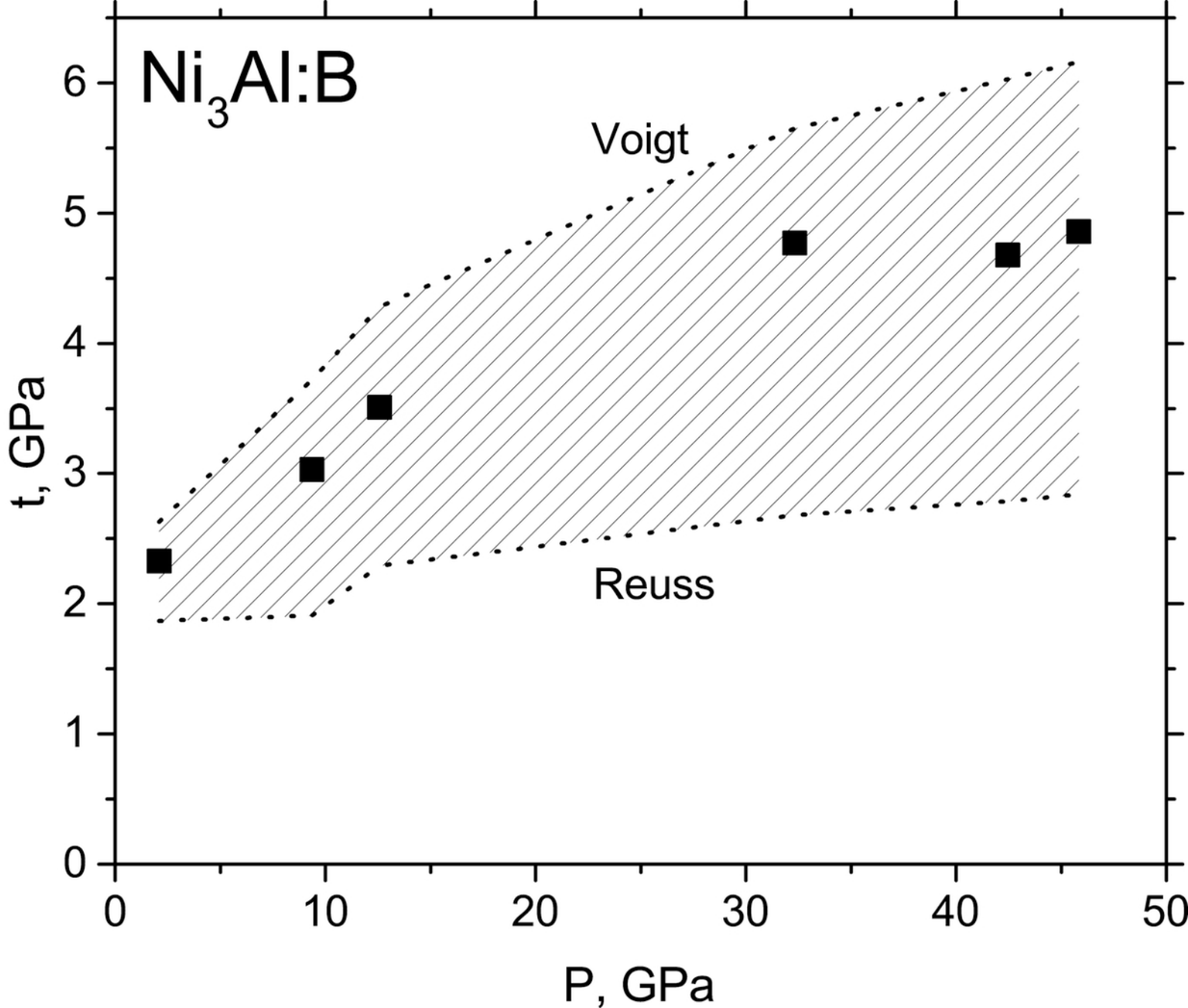
Ni3Al:B
Voigt
Reuss
t, GPa
P, GPa
0
1
2
3
4
5
6
0
10
20
30
40
50

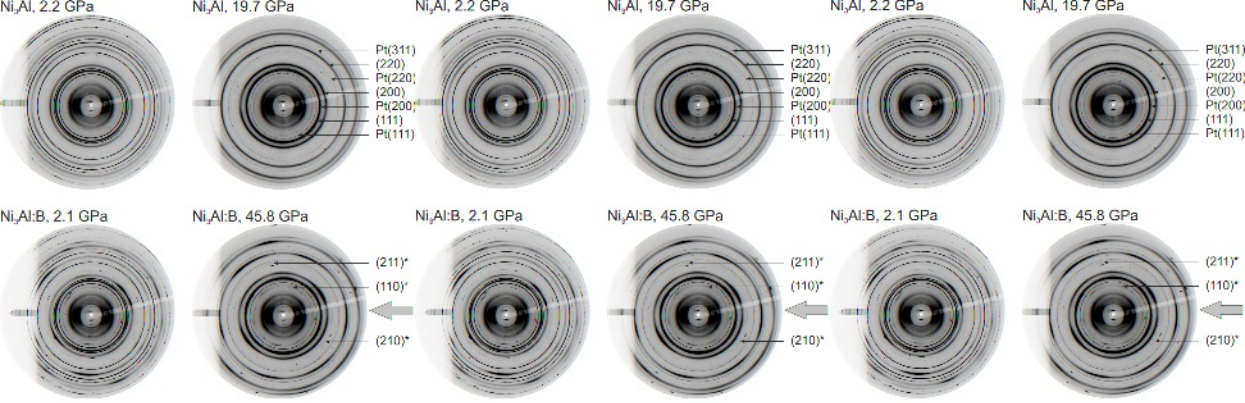
Ni3Al, 2.2 GPa
Ni3Al, 19.7 GPa
Pt(311)
(220)
Pt(220)
(200)
Pt(200)
(111)
Pt(111)
Ni3Al, 2.2 GPa
Ni3Al, 19.7 GPa
Pt(311)
(220)
Pt(220)
(200)
Pt(200)
(111)
Pt(111)
Ni3Al, 2.2 GPa
Ni3Al, 19.7 GPa
Pt(311)
(220)
Pt(220)
(200)
Pt(200)
(111)
Pt(111)
Ni3Al:B, 2.1 GPa
Ni3Al:B, 45.8 GPa
(211)*
(110)*
(210)*
Ni3Al:B, 2.1 GPa
Ni3Al:B, 45.8 GPa
(211)*
(110)*
(210)*
Ni3Al:B, 2.1 GPa
Ni3Al:B, 45.8 GPa
(211)*
(110)*
(210)*

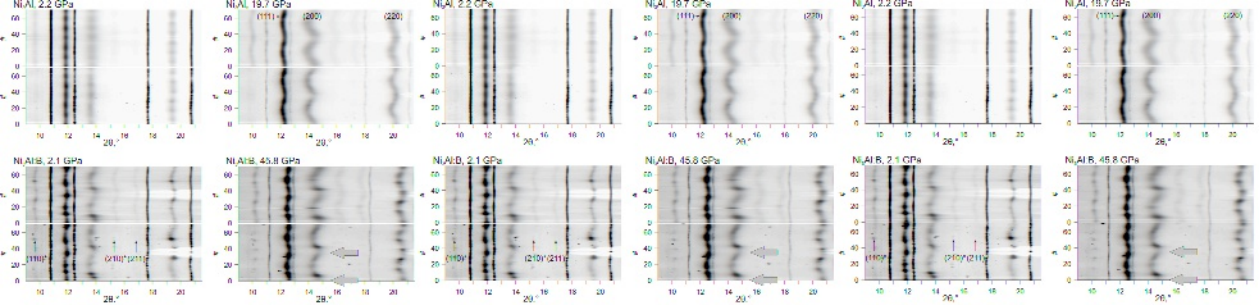
Ni3Al, 2.2 GPa
Ni3Al, 19.7 GPa
Ni3Al, 2.2 GPa
Ni3Al, 19.7 GPa
Ni3Al, 2.2 GPa
Ni3Al, 19.7 GPa
(111)
(200)
(220)
(111)
(200)
(220)
(111)
(200)
(220)
2θ,°
Ni3Al:B, 2.1 GPa
Ni3Al:B, 45.8 GPa
Ni3Al:D, 2.1 GPa
Ni3Al:D, 45.8 GPa
Ni3Al:B, 2.1 GPa
Ni3Al:B, 45.8 GPa
(110)*
(210)*/(211)
(110)*
(210)*/(211)
(110)*
(210)*/(211)
(110)*
(210)*/(211)
(110)*
(210)*/(211)
(110)*
(210)*/(211)
2θ,°

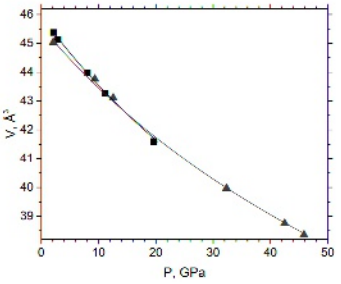
V, Å^3
P, GPa

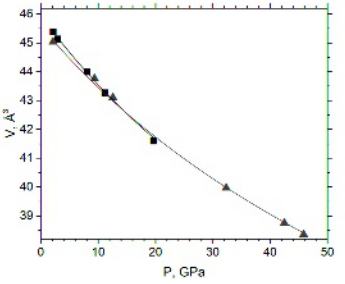
V, Å^3
P, GPa

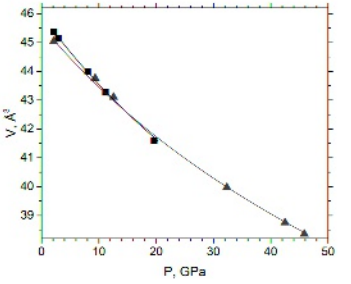
V, Å^3
P, GPa